Characteristics of High Efficiency Dye-Sensitized Solar Cells[†]

Qing Wang,[‡] Seigo Ito,[‡] Michael Grätzel,[*,‡] Francisco Fabregat-Santiago,[§] Iván Mora-Seró,[§] Juan Bisquert,[*,§] Takeru Bessho,[‡,||] and Hachiro Imai[||]

Laboratory for Photonics and Interfaces, Institute of Chemical Sciences and Engineering, Ecole Polytechnique Fédérale de Lausanne, 1015 Lausanne, Switzerland, Departament de Ciències Experimentals, Universitat Jaume I, 12071 Castelló, Spain, and Environmental Material Laboratory, Material Science of Engineering, Graduate School of Engineering, Shibaura Institute of Technology 3-9-14, Shibaura, Minatoku, Tokyo, Japan 108-8548

Received: July 6, 2006; In Final Form: September 19, 2006

Impedance spectroscopy was applied to investigate the characteristics of dye-sensitized nanostructured TiO$_2$ solar cells (DSC) with high efficiencies of light to electricity conversion of 11.1% and 10.2%. The different parameters, that is, chemical capacitance, steady-state transport resistance, transient diffusion coefficient, and charge-transfer (recombination) resistance, have been interpreted in a unified and consistent framework, in which an exponential distribution of the localized states in the TiO$_2$ band gap plays a central role. The temperature variation of the chemical diffusion coefficient dependence on the Fermi-level position has been observed consistently with the standard multiple trapping model of electron transport in disordered semiconductors. A Tafel dependence of the recombination resistance dependence on bias potential has been rationalized in terms of the charge transfer from a distribution of surface states using the Marcus model of electron transfer. The current−potential curve of the solar cells has been independently constructed from the impedance parameters, allowing a separate analysis of the contribution of different resistive processes to the overall conversion efficiency.

1. Introduction

After more than one decade of development, the photosensitization of wide-band gap nanocrystalline semiconductors by adsorbed dyes has become a realistic option for solar cell applications, and dye-sensitized solar cells (DSC) currently present the most promising alternative to the conventional solar cells.[1−5] The fundamental component of the DSC is a photoanode consisting of a monolayer of sensitizer (dye) adsorbed onto a mesoporous semiconductor oxide (typically TiO$_2$). In contrast to conventional solar cell systems, where the semiconductor assumes both the task of light absorption and charge carrier, in dye-sensitized solar cells light is absorbed by the anchored dye and charge separation takes place at the interface via photoinduced electron injection from the dye into the conduction band of the solid. In a porous film consisting of nanometer-sized TiO$_2$ particles, the effective surface area for dye adsorption can be greatly enhanced and efficient light absorption is achieved from dye monolayers. During the illumination of the cell, electrons are injected into the conduction band of TiO$_2$ by photoexcited dye molecules adsorbed on the nanoparticle surface, which is in contact with an electrolyte. Redox species in the electrolyte transport holes from the oxidized dye molecules to the counter electrode. Ruthenium polypyridyl complexes have proved to be the most efficient TiO$_2$ sensitizers, with the *cis*-RuL$_2$(SCN)$_2$ (L = 2,2′-bipyridyl-4,4′-dicarboxylic acid) dye (N3 dye) demonstrating incident photon-to-electron conversion efficiencies (IPCEs) of up to 85% from

400 to 800 nm, corresponding to almost unity quantum yield (electrons per absorbed photon) when light losses are taken into account.[2,6,7]

Pursuing high efficiency is always the core task for photovoltaic devices. For DSC, an overall energy conversion efficiency (η) of 11.0% has been achieved at AM 1.5.[6,7] However, it is still a big challenge approaching higher efficiency. Except for judicious molecular engineering of panchromatic sensitizers for enhanced light harvesting (especially in the near-infrared region),[3,8] it is believed that optimized mesoscopic TiO$_2$ films and dye-sensitized TiO$_2$−electrolyte interfaces for fast electron propagation and slow electron recombination are equally important for achieving higher efficiency. This is apparent from the fluctuated efficiencies of the same dye-sensitized cells with different films and electrolytes.

Impedance spectroscopy is a useful technique to investigate the kinetic processes of DSC.[9−18] At the proper conditions, electron transport in the mesoscopic TiO$_2$ film, electron recombination at the TiO$_2$−electrolyte interface, charge transfer at the counter electrode, and diffusion of the redox species in a electrolyte can be well distinguished according to the spectral shapes of the impedance response as a function of frequency. A series of recent papers has explored extensively the properties of DSC using impedance spectroscopy under different conditions of illumination, bias potential, electrolyte composition, and nanocrystalline TiO$_2$ preparation routes.[11,15,16,18] These works employ the diffusion−recombination model[10] for the electronic processes in the metal oxide and additional elements for the electrolyte and contact processes. Therefore, this model has been well established and can be considered a major tool for the practical characterization of the DSC. However, several important aspects of the interpretation of this model and the application

---

[†] Part of the special issue "Arthur J. Nozik Festschrift".
[*] To whom correspondence should be addressed.
[‡] Ecole Polytechnique Fédérale de Lausanne.
[§] Universitat Jaume I.
[||] Shibaura Institute of Technology.

High Efficiency Dye-Sensitized Solar Cells

J. Phys. Chem. B, Vol. 110, No. 50, 2006 **25211**

for determining the solar cell performance require further work, and this is the aim of the present paper.

Here, two highly efficient DSC with 10.2% and 11.1% power efficiency at AM 1.5 are characterized by this technique. The factors that influence the photovoltaic performance are discussed in light of the parameters derived from the impedance spectra. In addition, because of the ideal electron transport and recombination behaviors, these high efficiency cells provide a good platform to demonstrate the transport−recombination model. Compared with other techniques, such as photocurrent/photovoltage transient[19,20] and intensity modulated photocurrent spectroscopy (IMPS)/intensity modulated photovoltage spectroscopy (IMVS),[21−23] the advantage of impedance spectroscopy is that we can obtain all of the parameters at the same time, so we can test models by the correlation between parameters.

2. Experimental Section

2.1. Materials. 4-*tert*-Butylpyridine (Fluka), acetonitrile (Fluka), and valeronitrile (Fluka) were purified by vacuum distillation. Guanidinium thiocyanate (Aldrich) and H_2PtCl_6 (Fluka) were used as received. H_2O was purified by distillation and filtration (Milli-Q). $TiCl_4$ (Fluka) was diluted with water to 2 M at 0 °C to make a stock solution, which was kept in a refrigerator and freshly diluted to 40 mM with water for each $TiCl_4$ treatment of the FTO-coated glass plates. Iodine (Aldrich) was purified by sublimation. The syntheses of *cis*-di(thiocyanato)-*N,N'*-bis(2,2'-bipyridyl-4-carboxylic acid-4'-tetrabutylammonium carboxylate) ruthenium (II) (N-719) and butylmethylimidazolium iodide (BMII) were reported in our previous paper.[24,25] The chromatographic purification of N-719 was carried out three times on a column of Sephadex LH-20, using water as an eluant. Two kinds of TiO_2 paste containing nanocrystalline TiO_2 (20 nm, paste A) and submicroparticle TiO_2 (400 nm, paste B) were prepared by a previously reported procedure.[26]

2.2. Fabrication of Dye-Sensitized Solar Cells. For the DSC working electrodes, the FTO glass plates (solar 4 mm thickness, 10 Ω/□, Nippon Sheet Glass) were first cleaned in a detergent solution using an ultrasonic bath for 15 min and then rinsed with water and ethanol. After treatment in a UV−O_3 system (model no. 256-220, Jelight Company, Inc.) for 18 min, the FTO glass plates were immersed into 40 mM $TiCl_4$(aq) at 70 °C for 30 min and then washed with water and ethanol. The FTO glass plates were coated with a layer of paste A by screen printing (90T, Estal Mono, Schweiz. Seidengazefabrik AG Thal), kept in a clean box for 3 min so that the paste could relax to reduce surface irregularity, and then dried for 6 min at 125 °C. The screen characteristics are as follows: material, polyester; mesh count, 90T cm (or 230T inch/mesh); mesh opening, 60 μm; thread diameter, 50 μm; open surface, 29.8%; fabric thickness, 83 μm; theoretical paste volume, 24.5 cm³ m⁻²; K/KS volume, 17.0 cm³ m⁻²; weight, 48 g m⁻². This screen-printing procedure with paste A (coating, storing, and drying) was repeated 4 times to get an appropriate thickness, that is, 12−14 μm, for the working electrode. After drying paste A at 125 °C, paste B was deposited twice by screen printing, resulting in light-scattering TiO_2 films containing 400-nm-sized anatase particles of 2−5 μm thickness. The electrodes coated with the TiO_2 pastes were gradually heated under an air flow at 325 °C for 5 min, at 375 °C for 5 min, at 450 °C for 15 min, and then at 500 °C for 15 min. The surface images of the TiO_2 electrodes were obtained by an optical computing system and then integrated over the resulting image to analyze the surface area. After further treatment with 40 mM $TiCl_4$, the TiO_2 films were rinsed with water and ethanol and then sintered at 500 °C for 30 min. After cooling to 80 °C, the TiO_2 electrodes were immersed into the N-719 dye solution (0.5 mM in a mixture of acetonitrile and *tert*-butyl alcohol, 1:1 volume ratio) and then kept at room temperature for 20−24 h.

For the counter electrodes, the FTO plates (TEC 15 Ω/□, 2.2 mm thickness, Libbey-Owens-Ford Industries) were drilled by sand blasting, washed with H_2O and 0.1 M HCl in ethanol, and then subsequently cleaned in an ultrasonic bath with acetone for 10 min. After surface organic contamination was removed by heating at 400 °C for 15 min, the counter electrodes were prepared by coating with a drop of H_2PtCl_6 solution (2 mg of Pt in 1 mL of ethanol) on the FTO and then heating at 400 °C for 15 min.

The dye-stained TiO_2 films and the Pt counter electrodes were assembled into sealed sandwich-type cells by heating with a hot-melt of ionomer films (Surlyn 1702, 25 μm thickness, Du-Pont) used as spacers between the electrodes. A drop of electrolyte solution (0.60 M BMII, 0.03 M I_2, 0.10 M guanidinium thiocyanate, and 0.50 M 4-*tert*-butylpyridine in a mixture of acetonitrile and valeronitrile (85:15 volume ratio)) was put on each of the drilled holes in the counter electrodes of the assembled cells. Subsequently, the cells were put into a small chamber and the air in the chamber and inside the cells was pumped out for 5−10 s until the bubbling of the electrolyte was finished. Opening the chamber to air caused the electrolyte to be driven into the cell via vacuum backfilling. Finally, the holes were sealed using hot-melt ionomer films (Bynel 4702, 35 μm thickness, Du-Pont) and cover glasses (0.1 mm thickness). To remove the thin TiO_2 layer on the FTO and to have a good electrical contact for the connections to the measurement setup, the edge of the FTO outside of the cells was scraped with sandpaper or a file. A solder (Cerasolza, Asahi Glass) was applied on each side of the FTO electrodes. To prevent the collection of scattered light, masks made of black plastic tape were attached to the ARKTOP filter.

2.3. *i*−*V* Measurements. Photovoltaic measurements of the DSC employed an AM 1.5 solar simulator (100 mW cm⁻²) equipped with a Schott 113 filter between the sample and a 350 W xenon lamp. The power of the simulated light was calibrated by using a reference Si photodiode equipped with an IR-cutoff filter (KG-3, Schott) to reduce the mismatch in the region of 350−750 nm between the simulated light and the AM 1.5 to less than 2%.[3,27] The photovoltaic characteristics of DSC were obtained by applying an external potential bias to the cell and measuring the generated photocurrent with a Keithley model 2400 digital source meter. The voltage step and delay time of the photocurrent were 10 mV and 40 ms, respectively, in accordance with the report by Koide and Han.[28] It was confirmed that the *i*−*V* curve of the DSC showed no hysteresis under these conditions.

2.4. Electrochemical Impedance Measurements. Impedance measurements of cell A were performed with a computer-controlled AutoLab PSTA30 with a frequency range of 0.005−10⁵ Hz. Cell B was measured with a potentiostat (EG&G, M273) equipped with a frequency response analyzer (EG&G, M1025), with the frequency range being 0.05−10⁵ Hz. The magnitude of the alternative signal was 10 mV. The impedance measurements were carried out under different voltage biases in the dark and under AM 1.5 solar radiation.

3. Results and Discussion

3.1. Photovoltaic Performance. The photocurrent−voltage characteristics of the two efficient DSC are shown in Figure 1.

25212 *J. Phys. Chem. B, Vol. 110, No. 50, 2006*

Wang et al.
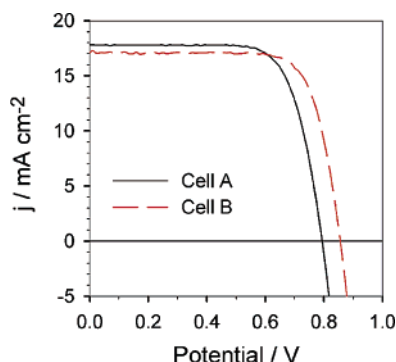
Figure 1. Photocurrent−voltage characteristics of two DSC. The sensitizer used was N-719. The electrolyte consisted of 0.60 M BMII, 0.03 M I_2, 0.10 M guanidinium thiocyanate, and 0.50 M 4-*tert*-butylpyridine in a mixture of acetonitrile and valeronitrile (85:15 volume ratio). The film thickness consists of a 12 μm transparent layer plus a 2 μm (cell A) or a 4 μm (cell B) scattering layer. The overall energy conversion efficiencies of cells A and B are 10.2% (V_{oc}, 795 mV; J_{sc}, 17.48 mA/cm^2; *ff*, 0.733) and 11.1% (V_{oc}, 856 mV; J_{sc}, 17.05 mA/cm^2; *ff*, 0.759), respectively. A light source simulating global AM 1.5 solar radiation was employed.

With the Ru complex N-719 as the photosensitizer, the overall energy conversion efficiencies of cells A and B were measured under AM 1.5 solar radiation to be 10.2% (V_{oc}, 795 mV; J_{sc}, 17.48 mA/cm^2; *ff*, 0.733) and 11.1% (V_{oc}, 856 mV; J_{sc}, 17.05 mA/cm^2; *ff*, 0.759), respectively, where the electrolyte consisted of 0.60 M BMII, 0.03 M I_2, 0.10 M guanidinium thiocyanate and 0.50 M 4-*tert*-butylpyridine in a mixture of acetonitrile and valeronitrile (85:15 volume ratio). These values are close to the highest efficiencies reported for the DSC so far.[7,29,30] Compared with other less efficient cells, the outstanding parameter is the high open circuit photovoltage, exceeding 850 mV for cell B. At the same time, the reasonable value for the short circuit photocurrent and the excellent fill factor render these cells highly efficient. In the following discussion, impedance spectroscopy will be employed to discover the origins of this superb photovoltaic performance.

3.2. Impedance Results. Cells A and B were characterized by impedance spectroscopy in the dark at different temperatures and forward biases. As shown in Figure 2, the impedance spectra of cell B present the characteristic kinetic processes of DSC in different frequency domains. With a decrease in the bias potential from 0.70 V to 0.60 V, electron transport in the mesoscopic TiO$_2$ film appears as a distinguished Warburg-like diffusion behavior in the high-frequency region and the interfacial charge recombination process grows to a large semicircle in the low-frequency region.

In the dark, the DSC behave as a leaking capacitor.[10] Upon forward bias, the electrons are injected from the FTO substrate into the TiO$_2$ and the film is charged by electron propagation through the mesoscopic TiO$_2$ network. Meanwhile, a fraction of the injected conduction band electrons are lost by the reduction of I$_3^-$ ions present in the electrolyte. These electronic processes in the DSC are well described by a transmission line model, as shown in Figure 3, where the model developed in previous works[10,15] has been completed with recent results from Hosikawa.[17] In the transmission line, there are two channels in parallel, representing electron transport through TiO$_2$ and redox species transport in the electrolyte in the pores, respectively. The charge-transfer process related to the reaction of the electrons with the I$_3^-$ ions at the TiO$_2$−electrolyte interface connects these two channels. If L is the thickness of the mesoscopic TiO$_2$ film, the electron transport resistance in the

TiO$_2$ film is R_t (= $r_t L$), while the interfacial charge recombination resistance is R_{ct} (= r_{ct}/L).

Clearly, the spectra of cell B show the ideal characteristics of the diffusion−recombination model with $R_{ct} \gg R_t$.[10,15] Inspection of the spectra reveals that the fraction R_{ct}/R_t is so large that the efficiency is not affected by the diffusion at such high bias.

The bias potential relates to the electrochemical potential of the electrons, E_{Fn}, as $V = (E_{Fn} - E_{F,redox})/e$, where e is the elementary charge and $E_{F,redox}$ is the redox potential in the electrolyte, that equals the electron Fermi level at $V = 0$, E_{F0}. Since E_{Fn} is practically homogeneous under the measurement conditions used in this work, it will be denoted, hereafter, as the electron Fermi level. It should be noted that, in the dark, the infrared (IR) drop across the resistances contributing in series during the impedance measurement is negligible as the current passing through the cell is very small (<0.03 mA) at the applied bias potentials. Thus, these potentials were taken directly without further correction. Similarly, it can be calculated that, in the dark, the Fermi level through the mesoscopic TiO$_2$ film remains almost flat at various forward biases, because of the small potential drop ($I_{dark}R_t$).

The chemical capacitance C_μ (= $c_\mu L$) reflects the change of electron density on a small variation of the chemical potential. For a given Fermi level, it has the form[31,32]

$$C_\mu = e^2 \frac{\partial}{\partial E_F} \int_{E_2}^{E_1} F(E - E_{Fn})g(E)dE \approx e^2 g(E_F) \qquad (1)$$

where $F(E - E_{Fn})$ is the occupation factor given by the Fermi−Dirac distribution function and $g(E)$ is the density of states. A common finding in nanostructured TiO$_2$ is an exponential distribution of the localized states in the band gap,[33,34] as described by the expression

$$g(E) = \frac{N_L}{k_B T_0} \exp[(E - E_c)/k_B T_0] \qquad (2)$$

Here, N_L is the total density of the localized states and T_0 is a parameter with temperature units that determines the depth of the distribution below the lower edge of the conduction band, E_c. The precise location of the exponential distribution of the traps (eq 2) in nanostructured TiO$_2$ has not been established to date. There are few traps, typically one,[35] within an isolated TiO$_2$ nanoparticle. When they are made into a nanocrystalline film, the necking between the particles affects their electronic structure. Hence, it is very plausible that these traps are mainly located at the particle−particle contact. In addition, Ti(IV) surface states could act as electron traps. However, the energy of the latter states depends on surface protonation and may be raised into the conduction band by dye adsorption or proton removal. Hence, their role as an electron trap is questionable.

The density of states in nanostructured TiO$_2$ films has been measured by several methods, such as cyclic voltammetry (CV), and the results are consistently described by eq 2 with a good approximation.[36−38] However, the measurements of the capacitance from impedance spectroscopy, or CV and similar methods, only probe the Fermi level at the substrate, which is determined by an average of the electronic states in the whole film. It is, therefore, not possible to obtain a spatial resolution of the position of the traps in the nanoparticles by these methods, nor is it possible to determine their origin. A theoretical explanation of eq 2 has been presented in terms of the effects of impurities and dielectric mismatch at the boundary between the semiconductor nanoparticle and the surrounding medium[39,40] over the

High Efficiency Dye-Sensitized Solar Cells

J. Phys. Chem. B, Vol. 110, No. 50, 2006 **25213**
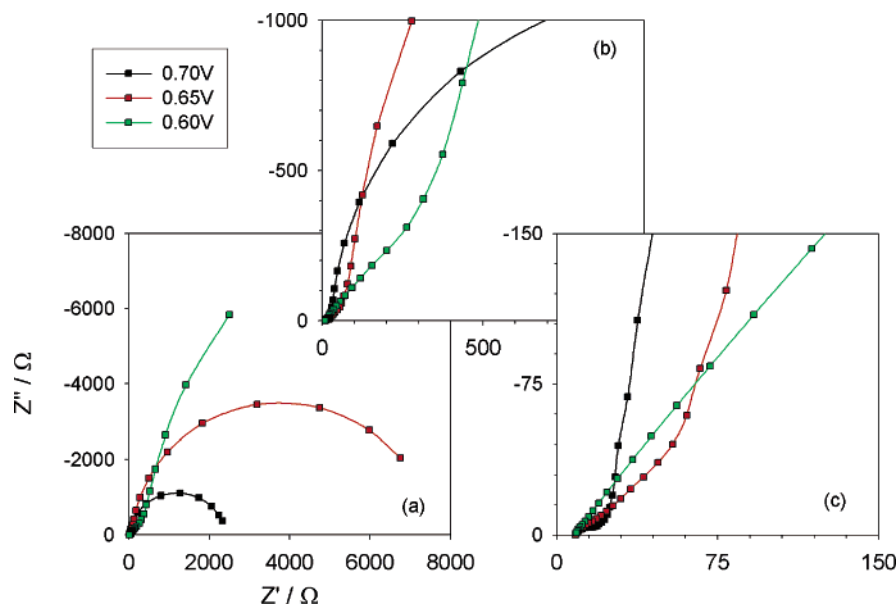
Figure 2. Impedance spectra of cell B at forward biases of 0.60, 0.65, and 0.70 V in the dark. The enlarged spectra of (a) are shown in (b) and (c).
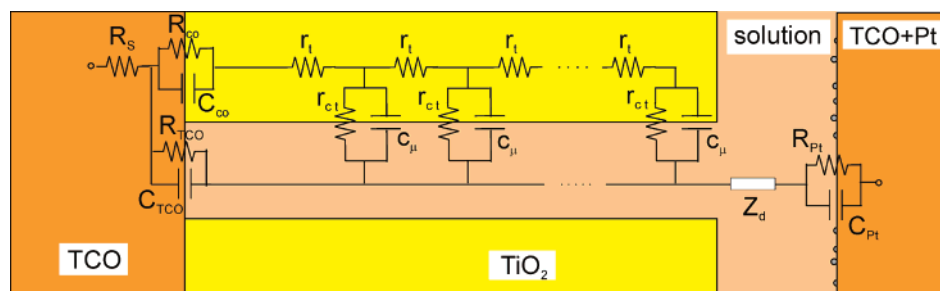
Figure 3. General transmission line model of DSC. r_{ct} is the charge-transfer resistance of the charge recombination process between electrons in the mesoscopic TiO_2 film and I_3^- in the electrolyte; C_μ is the chemical capacitance of the TiO_2 film; r_t is the transport resistance of the electrons in the TiO_2 film; Z_d is the Warburg element showing the Nernst diffusion of I_3^- in the electrolyte; R_{Pt} and C_{Pt} are the charge-transfer resistance and double-layer capacitance at the counter electrode (platinized TCO glass), respectively; R_{TCO} and C_{TCO} are the charge-transfer resistance and the corresponding double-layer capacitance at the exposed TCO−electrolyte interface, respectively; R_{CO} and C_{CO} are the resistance and the capacitance at the TCO−TiO_2 contact, respectively; R_s is the series resistance, including the sheet resistance of the TCO glass and the contact resistance of the cell. L is the thickness of the mesoscopic TiO_2 film.

electron wave functions. Some recent papers[41,42] have also emphasized the role of impurities in the nanoparticles and indicated that traps are located predominantly at the particle interface. It appears that the most salient manifestation of the traps in nanostructured TiO_2 is their effect on the dynamics of electrons, such as electron transport and interfacial charge transfer. Therefore, in the following, eq 2 will be adopted to develop detailed models for electron transport and recombination that explain the experimental results, which support the assumption of the exponential distribution; however, we note that microscopic information about electron traps cannot be obtained by these methods.

The capacitance measured by impedance spectroscopy is, in fact, the sum of the capacitance contributed by the electronic states (C_μ) and the space charge (C_{sc}) on the semiconductor side and by the Helmholtz layer (C_H) and the surface adsorbed ionic species (C_{ad}) on the electrolyte side, where C_μ and C_{sc}, C_H and C_{ad} are in parallel ($C_\mu||C_{sc}$-$C_H||C_{ad}$), respectively. Since there is no space charge region for nanocrystalline TiO_2, C_{sc} can be neglected within the entire potential region. The double-layer capacitance ($C_H||C_{ad}$) has only a small contribution to the total capacitance at the higher bias potentials.

In addition to the elements in the transmission line, there are other elements in the equivalent circuit model that describe additional processes in the DSC: the charge-transfer resistance R_{Pt} and the interfacial capacitance C_{Pt} at the platinized counter electrode−electrolyte interface, the charge-transfer resistance R_{TCO} for electron recombination from the uncovered layer of the conducting glass (TCO) to the electrolyte, the sheet resistance R_S of the TCO, the capacitance C at the exposed FTO−electrolyte interface, the resistance R_{CO} and the capacitance C_{CO} at the TCO−TiO_2 contact, and, finally, the impedance $Z_{d(sol)}$, with the direct current (dc) resistance R_D showing the diffusion of redox species in the electrolyte.[11] All impedance spectra in this study were fitted with this transmission line model. For better fitting, all capacitor elements were replaced by constant phase elements that, in any case, keep the constant phase element (CPE) exponent γ_μ quite close to the perfect capacitor value, $\gamma_\mu \approx 1$. From the fitted data, we could calculate the evolution of parameters such as the electron diffusion coefficient $D_n = (R_t C_\mu)^{-1}$, the lifetime $\tau_n = R_{ct} C_\mu$, and the effective diffusion length $L_n = (D_n \tau_n)^{1/2}$. At the potentials measured, R_{TCO} and C_{TCO} were negligible and, at only 1 sun illumination, a small effect of diffusion in the electrolyte appeared.

Figure 4 presents the fitting results of the parameters of the capacitance and transport of the two cells measured in the dark at different forward biases and temperatures.
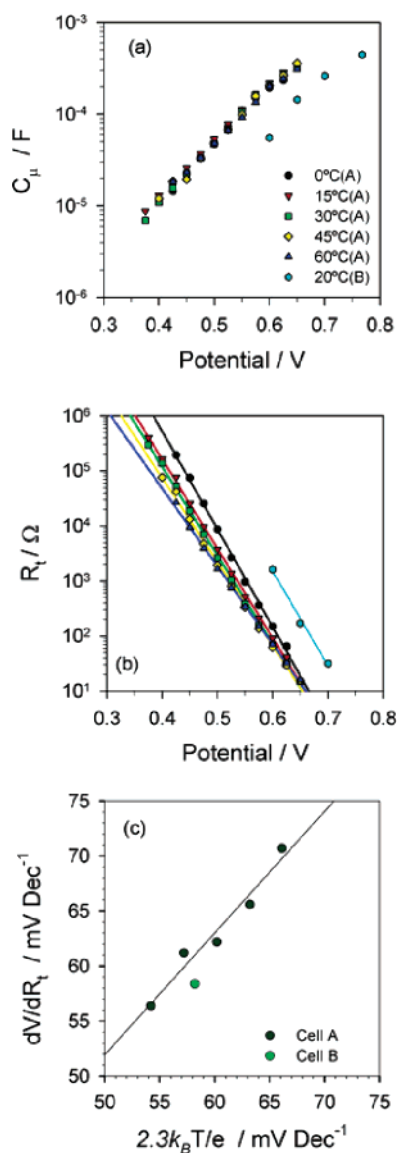
Figure 4. (a) Chemical capacitance C_μ and (b) electron transport resistance R_t obtained from impedance in the dark. (c) Comparison between the experimental and theoretical values of $\partial \log R_t/\partial V$ of cells A and B.

According to eqs 1 and 2, an exponential distribution of the localized states in the band gap of TiO$_2$, with a characteristic temperature T_0, gives the chemical capacitance

$$C_\mu = C_0 \exp\left(\frac{\alpha e}{k_B T} V\right) = C_0 \exp\left(\frac{e}{k_B T_0} V\right) \qquad (3)$$

where the coefficient $\alpha = T/T_0$. Accordingly, $C_\mu(V)$ should be independent of temperature and the slope $\partial \ln C_\mu/\partial V$ should have a constant value of $e/k_B T_0$. This is fairly consistent with the experiment results. As shown in Figure 4a, the obtained chemical capacitance of cell A barely changes with the temperature within the potential range. In terms of the slope of C_μ, α is calculated to be 0.36–0.40, and $e/k_B T_0$ is ~166 mV/dec, which is much larger than that obtained by Frank et al.[23] When the bias potential is higher than 0.55 V, the slope decreases slightly, because of a small contribution by $C_H||C_{ad}$. In addition, from the larger slope at a lower potential, cell B has a larger α compared to that of cell A.

As shown in Figure 4b, the transport resistance, R_t, is characterized by an exponential dependence with bias with a

slope that changes with the temperature. This dependence indicates the presence of a transport level that, hereafter, will be identified with the lower edge of the conduction band, E_c. If the temperature dependence of the mobility is neglected, then the transport resistance is inversely proportional to the density of carriers at the transport level, which is governed by the Boltzmann distribution, provided that $E_F \ll E_c$. Therefore,[15]

$$R_t = R_{t0} \exp\left[-\frac{e}{k_B T}\left(V + \frac{E_{F,redox} - E_c}{e}\right)\right] \qquad (4)$$

In Figure 4a and b, the data from sample B are shifted from those of sample A. This shift, +70 mV in both cases, may be explained by eqs 2 and 4 as a shift in the conduction band edge of TiO$_2$, E_c, toward higher values in cell B, and it is in quite good agreement with the higher open circuit photovoltage (+61 mV) found for this sample.

On the other hand, at a fixed conduction band edge, the dependence of the transport resistance on the bias potential is given by the thermal energy $k_B T$. In terms of the fitted slope $\partial \log R_t/\partial V$, Figure 4c compares the experimental slopes of R_t obtained from Figure 4b at various temperatures with the theoretical values ($-e/2.303k_B T$). For cell A, the experimental slope values are very close to those predicted by eq 4. In Figure 4c, the average ratio is 1.06, suggesting that the motion of electrons is limited by the rate of thermal excitations to a well-defined transport level, a question that is further discussed below. The slope of R_t for cell B is 58.4 mV/dec at 20 °C, which is almost identical to the theoretical value of 58.2 mV/dec. Since the measured transport resistance is an averaged value of the local contributions over the whole semiconductor, obtaining the ideal statistics indicates that the Fermi level is practically homogeneous, as assumed in the impedance model. This indicates excellent potentiostatic control of the Fermi level in the semiconductor film from the substrate.[43]

From the point of intersection of all the tendency lines of R_t in cell A (Figure 4b), the position of the conduction band edge is obtained as $V_{cb} \approx 0.75$ V. This value is below the open circuit potential found at 1 sun illumination (0.80 V), indicating that some shift of the conduction band edge occurs at high applied potentials due to the contribution by the surface polarization with $C_H||C_{ad}$.

The results on chemical capacitance and transport resistance are consistent with a classical multiple trapping (MT) model for electron transport,[44] which is indicated schematically in Figure 5a. In this approach, the total electron density is composed of electron densities in a conduction band n_c (with an effective density of states (DOS) N_c) and in localized states n_L. Transport through extended states is slowed by trapping–detrapping events to localized states, while direct hopping between localized states is neglected. Figure 5b quantitatively shows the equilibrium carrier distribution in the band gap. It is observed that the overall distribution is not significantly affected by the temperature variation from 300 to 400 K, provided that the Fermi level is fixed. In both cases, the majority of the carrier density lies in the energy region around the Fermi level, which explains the stationary values of the chemical capacitance in Figure 4a. However, the density of electrons at E_c increases markedly with an increase in temperature. It should be noted that the transport resistance in the MT framework relates to the dc transport and is not affected by trapping–detrapping events.[13] Hence, R_t indicates the density of carriers at the conduction band, which does increase with the temperature as noted before. Activation energies of the transport resistance are reported in the Supporting Information.

High Efficiency Dye-Sensitized Solar Cells

J. Phys. Chem. B, Vol. 110, No. 50, 2006 **25215**
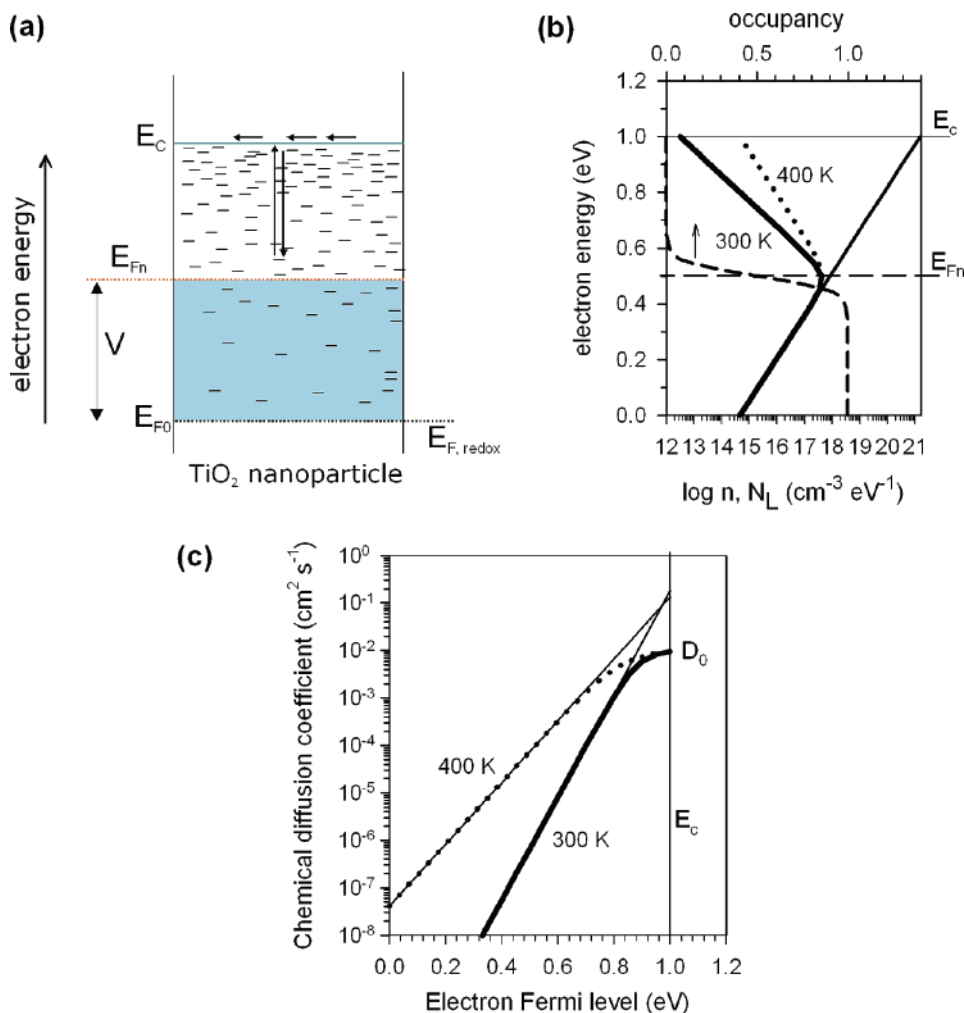
Figure 5. (a) Schematic energy diagram of the electronic processes governing electron transport in a TiO$_2$ nanoparticle in DSC. E_{F0} shows the position of the Fermi level in the dark, which is equilibrated with the redox potential ($E_{F,redox}$) of the iodide−triodide couple. E_{Fn} is the Fermi level of the electrons accumulated in the nanoparticles, and E_C is the conduction band energy. The shaded region indicates the band gap states that are occupied by electrons below the Fermi level (zero-temperature approximation of the Fermi−Dirac distribution). The arrows show the transport of the electrons at the transport level and at a trapping−detrapping event. (b) Quantitative representation of the thermal occupation at $T = 300$ K (thick line) of an exponential DOS in the band gap (thin line) with $T_0 = 800$ K and $N_L = 10^{20}$ cm^{-3}, as determined by the Fermi−Dirac distribution function (dashed line). The dotted line indicates the distribution of the carriers at $T = 400$ K. (c) Quantitative representation of the chemical diffusion coefficient of the electrons in the multiple trapping model, assuming the density of the transport states $N_c = 7 \times 10^{20}$ cm^{-3} and $D_0 = 0.01$ cm^2 s^{-1}. The thin lines indicate the exponential dependence on the Fermi level.

The chemical diffusion coefficient, D_n, is the diffusion coefficient that is measured in transient methods.[13] Using the quasi-static approximation,[13] it can be shown that the chemical diffusion coefficient in the MT framework contains, in addition to the diffusion coefficient at the transport level, D_0, another factor related to the local equilibration of charge in the energy axis:

$$D_n = \frac{1}{1 + \dfrac{\partial n_L}{\partial n_c}} D_0 \qquad (5)$$

The term $\partial n_c/\partial n_L$ in eq 5 is the relationship of the free to trapped number of electrons for a small variation of the Fermi level. If this term is small, which occurs when $E_{Fn} < E_c - k_BT$, eq 5 reduces to the expression

$$D_n = \left(\frac{\partial n_c}{\partial n_L}\right) D_0 \qquad (6)$$

The prefactor $\partial n_c/\partial n_L$ describes the delay of the response of

the chemical diffusion coefficient, with respect to the free electron diffusion coefficient, by the trapping and detrapping process.[13] The calculation of the chemical diffusion coefficient in eq 6 for an exponential distribution gives an exponential dependence on the Fermi-level position as follows:[45]

$$D_n = \frac{N_c T_0}{N_L T} \exp\left[(E_{Fn} - E_c)\left(\frac{1}{k_B T} - \frac{1}{k_B T_0}\right)\right] D_0 \qquad (7)$$

The functional dependence in eq 7 is a consequence of the exponential variation of the time constant for detrapping when the Fermi level scans the band gap in Figure 5a. On another hand, the MT model (eq 5) also predicts that, when $(\partial n_c/\partial n_L) \geq 1$ at $E_{Fn} \approx E_c - k_BT$, $D_n \approx D_0$; that is, the chemical diffusion coefficient should coincide with the constant diffusion coefficient of the free electrons at the transport level. This is due to trap saturation that removes the variation of D_n with the Fermi level. The complete dependence of the chemical diffusion coefficient on the Fermi level position in this model, at different temperatures, is illustrated in Figure 5c.

Measurements of the electron (chemical) diffusion coefficient in DSC have been realized by small perturbations over different
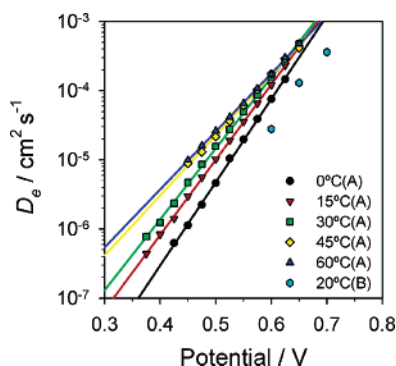
Figure 6. Chemical diffusion coefficients obtained from R_t and C_μ at different bias potentials and temperatures.

steady states using a variety of techniques: IMPS,[21,22] time-resolved photocurrents,[46] and impedance spectroscopy.[15,47] All of these results have found an exponential dependence of D_n either on bias voltage or on steady-state illumination, which has been generally rationalized in terms of the MT model with an exponential density of states.[21] The highest values measured barely exceed 2×10^{-4} cm^2 s^{-1}.[22,46] Additional experimental confirmation of the MT theory exposed above was reported by van de Lagemaat et al.[48] However, the validity of the MT model has, thus far, not been established by a temperature dependence of the slope of log $D_n(E_F)$, which is given by $[1 - \alpha(T)]/k_B T$, according to eq 7. Recent results by Kopidakis et al.[49] failed to find any temperature dependence of log $D_n(E_F)$. It should be noted that the linearity of α with the temperature is a classical landmark of the MT model in amorphous semiconductors.[50]

Our experimental results on $D_n(E_F)$, shown in Figure 6, are in very good agreement with the MT model. This is, to our knowledge, the first confirmation of MT electron transport in DSC by the temperature dependence of the slope $[1 - \alpha(T)]/k_B T$. We should point out that the determination of D_n by impedance spectroscopy is supported by the spectral shape of the impedance shown in Figure 2, which, moreover, warrants that the steady-state distribution of the electrons in the TiO$_2$ film is fairly homogeneous, as already mentioned, so that D_n-(E_F) is univocally determined. Furthermore, the maximal values measured for D_n (4×10^{-4} cm^2 s^{-1}) at room temperature exceed those reported before, which is another distinctive feature of the high-efficiency solar cells described here.

In common with all previously reported measurements by small perturbations over steady-state techniques, the data in Figure 6 show the variation of $D_n(E_F)$ corresponding to the region of trapping−detrapping in MT transport (eq 5) but not to the region of free-electron transport with a constant D_0 implicit in the model, as shown in Figure 5c at $E_F \approx E_c$. It appears that the electron diffusion coefficient D_0, corresponding

to the Fermi level reaching the transport level, has not been determined by any of the measurements of this type. There are several possible reasons for this: It is well-known[51] that when the electron density in the TiO$_2$ nanoparticles becomes large, the corresponding ionic charge in the surface produces a displacement of the semiconductor energy levels with respect to the electrolyte energy levels. Therefore, increasing E_F also produces a displacement of E_C, which is known as the band unpinning effect. Because of this effect, it is difficult to approach the semiconductor conduction band with the Fermi level, since the former starts to move when the latter becomes close.

In addition, in impedance spectroscopy measurement, the Warburg feature associated with electron transport becomes ummeasurably small at very negative potentials. Measurements of the electron conductivity, using an electrochemical transistor configuration, show the saturation of the conductivity when the Fermi level approaches the conduction band,[52] but a detailed interpretation of this effect in terms of the transport mechanism has not been provided. Therefore, direct proof of the existence of a transport level for electron transport in nanostructured TiO$_2$ permeated with a conductive medium, and the value of D_0 thereof, remains elusive.

By observing the features of the MT model in Figure 5c, it is noted that the lines log $D_n(E_F)$ at different temperatures intercept at an activationless point. This point is close but below E_c because of the T-prefactor in eq 7. With reference to the experimental data in Figure 6, we observe that the intercept places an upper constraint on the free electron diffusion coefficient, $D_0 = 10^{-2}$ cm^2 s^{-1}. We note again that the transport mechanism in the energy region where D_0 should be separately observed is not accessed in our measurements; however, it is not reasonable to expect a substantial increase of D_n in the region where $E_{Fn} \approx E_c$, with respect to the MT prediction. Therefore, the experimental data indicate that the free electron diffusion coefficient stands in a window where 4×10^{-4} cm^2 s$^{-1} \leq D_0 \leq 10^{-2}$ cm^2 s^{-1}. These values are in agreement with the results of high-frequency techniques,[53−58] summarized in Table 1, that probe the ultrafast relaxation of the electrons into TiO$_2$ nanoparticles. It should be noticed that the suggested values for trap-free electron diffusion in nanoporous TiO$_2$ are, in general, much lower than those of single-crystal or compact-film TiO$_2$,[53] as shown in Table 1.

Charge-transfer resistance dependence on potential and temperature is presented in Figure 7(a). It follows an exponential behavior similar to the Tafel law

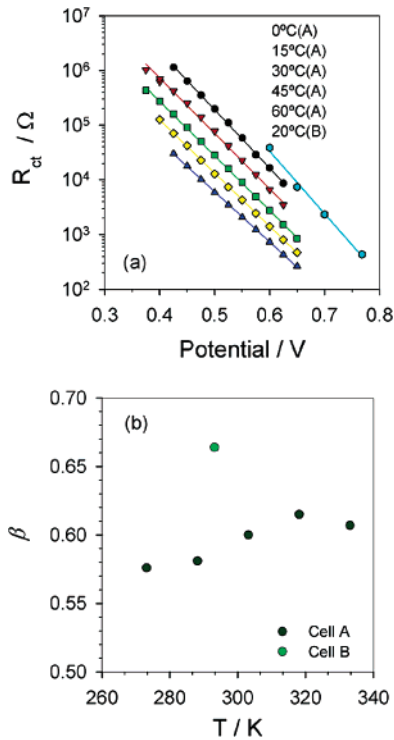$$R_{ct} = A \exp\left[-\frac{e\beta}{k_B T}V\right] \qquad (8)$$

with A and β being constants. The transfer coefficient β increases with an increase in temperature, as shown in Figure 7b.

TABLE 1: Electron Mobilities in TiO$_2$[a]

TiO$_2$ type	mobility (cm^2 V^{-1} s^{-1})	D_0 (cm^2 s^{-1})	technique
large single crystal n-type anatase	20	0.5	four-probe dc resistivity[53]
1.5 μm film n-type anatase	4	0.1	Hall mobility[54]
Degussa 25 nm diameter particle	1.5	4×10^{-2}	terahertz spectroscopy[55]
Degussa 25 nm diameter particle	0.01	3×10^{-4}	terahertz spectroscopy[56]
anatase 9 nm diameter particle	0.034	9×10^{-4}	microwave conductivity[57]

[a] $T = 300$ K.

High Efficiency Dye-Sensitized Solar Cells

J. Phys. Chem. B, Vol. 110, No. 50, 2006 **25217**

Figure 7. (a) Electron recombination resistance (R_{ct}) of cells A and B at different forward biases and temperatures. These parameters were obtained by fitting the impedance spectra of the cells measured in the dark. (b) Charge-transfer coefficients (β) of cells A and B obtained from (a).

The interpretation of the value of $\beta \approx 0.6$ found in Figure 7b is not immediately clear in terms of the models that describe the charge transfer between semiconductor nanoparticles and redox acceptors.[59,60] The direct transfer of electrons from the conduction band to the redox couple, which has been suggested in previous works at potentials close to the conduction band level,[32,60] demands a value of $\beta \approx 1$.

Another suggested mechanism is the electron transfer from a distribution of surface states $g_s(E)$ toward the electrolyte.[32,59,60] The probability of isoenergetic transfer from a surface state at the energy level E to an acceptor species in the electrolyte with concentration c_{ox} is given by the expression of the Marcus model

$$v_{el}(E) = k_0 \frac{2c_{ox}k_BT}{\sqrt{4\pi\lambda k_BT}} \exp\left[-\frac{(E - E_{F,redox} - \lambda)^2}{4\lambda k_BT}\right] \quad (9)$$

where k_0 is a time constant for tunneling and λ is the reorganization energy. The current per unit macroscopic area of an electrode of thickness L is

$$j_{rec}(E_{Fn}) = eL \int_{E_{F,redox}}^{E_c} g_s(E)F(E - E_{Fn})v_{el}(E)\, dE \quad (10)$$

The equilibrium occupancy of the surface states in the semiconductor is described by the Fermi−Dirac distribution function:

$$F(E - E_{Fn}) = \frac{1}{1 + \exp[(E - E_{Fn})/k_BT]} \quad (11)$$

The recombination resistance is

$$R_{ct}^{-1} = \frac{dj_{rec}(E_{Fn})}{dV} = -e^2L \int g_s(E)v_{el}(E) \frac{dF(E,E_{Fn})}{dE_{Fn}}\, dE \quad (12)$$

Note that

$$\frac{dF(E,E_{Fn})}{dE_{Fn}} = -\frac{dF(E,E_{Fn})}{dE} \quad (13)$$

Equation 13 is introduced in eq 12, and the latter can be integrated by parts. Applying the zero temperature limit of the Fermi−Dirac distribution, the following result is obtained:

$$R_{ct}(E_{Fn}) = [e^2 L g_s(E_{Fn})v_{el}(E_{Fn})]^{-1} \quad (14)$$

Assuming that $g_s(E)$ has the exponential form of eq 2 with parameters N_s and T_0, the resistance in eq 14 takes the form

$$R_{rec}(E_{Fn}) = R_0 \exp\left[\frac{(E_{Fn} - E_{redox} - \lambda)^2}{4\lambda k_BT} - \frac{E_{Fn} - E_c}{k_BT_0}\right] \quad (15)$$

where

$$R_0 = \frac{T_0\sqrt{\pi\lambda k_BT}}{e^2 L k_0 c_{ox} N_s T} \quad (16)$$

Equation 15 can also be expressed as

$$R_{rec}(E_{Fn}) = R_0 \exp\left[\frac{(E_{Fn} - E_{F,redox} - E_\mu)^2}{4\lambda k_BT} + \frac{E_c - E_{F,redox} - \lambda(1 + \alpha)}{k_BT_0}\right] \quad (17)$$

where

$$E_\mu = \lambda(1 + 2\alpha) = \lambda(1 + 2T/T_0) \quad (18)$$

According to eq 17, the resistance dependence on voltage, $V = e(E_{Fn} - E_{F,redox})$, consists of a Gaussian function centered at the energy E_μ indicated in eq 18. (A similar result was first given in ref 60.) The center E_μ of the Gaussian is shifted to a negative potential, with respect to the point of maximum (activationless) charge transfer at $E_{ox} = E_{Fn} - E_{F,redox} = \lambda$, by the amount $2\lambda\alpha$; in other words, $E_\mu = E_{ox} + 2\lambda\alpha$. The behavior of $R_{rec}(E_{Fn})$ in this model is illustrated In Figure 8. When the Fermi level is sufficiently below the minimum E_μ, eq 17 can be approximated as an exponential dependence,

$$R_{rec}(E_{Fn}) = R'_0 \exp\left[-\beta_1 \frac{(E_{Fn} - E_{F,redox})}{k_BT}\right] \quad (19)$$

where

$$\beta_1 = \frac{1}{2} + \alpha(T) \quad (20)$$

Therefore, this model satisfactorily explains the Tafel dependence indicated in eq 8. In addition, β_1 is predicted to increase linearly with the temperature, and this is, in fact, found in Figure 7b. However, the model simulations in Figure 8a indicate that R_{ct} must show some bending as the Fermi level approaches E_μ, which is not appreciated in Figure 7b. To investigate in more detail the application of this model, a series of impedance measurements were taken over a broader potential window at different aging treatments of cell A, and the experimental data are shown as points in Figure 9. The data displayed a modest bending at very high potentials and were
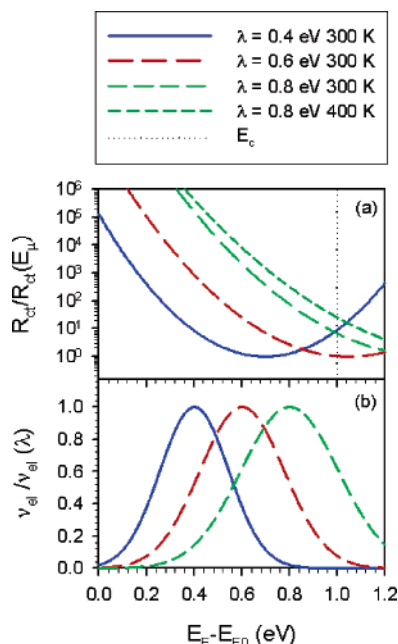
Figure 8. Model simulations of (a) the electron recombination resistance (R_{ct}) normalized to the minimum value, as a function of the Fermi level position, for the model of charge transfer in an exponential distribution of the surface states with the parameter $T_0 = 800$ K and (b) the charge-transfer probability normalized to the maximum value, as a function of the Fermi level position. Results are shown for the different values of the reorganization energy, λ, at $T = 300$ K and at different temperatures in the case where $\lambda = 0.8$ eV. The position of the conduction band, E_c, is indicated.
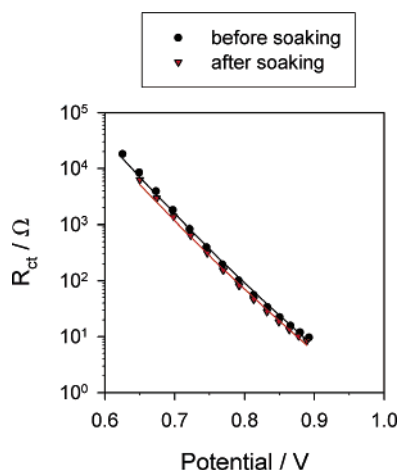

Figure 9. Charge-transfer resistance of sample A as a function of the bias potential (corrected from the iR drop due to series resistance) before and after aging treatment. The lines are fitted to the surface states charge-transfer model described in the main text. A slight displacement of R_{ct} determines the lower V_{oc} found for the aged sample.

TABLE 2: Data Obtained from the Fits of the Charge-Transfer Resistance Assuming Electron Recombination through a Distribution of Surface States

sample	α	β	λ (eV)
0 °C before light soaking	0.20	0.70	2 ± 1.2
0 °C after light soaking	0.19	0.69	1.9 ± 1.2

fitted to eq 17, taking the α values from the capacitance. The results of the fit are shown as lines in Figure 9, and the parameters are given in Table 2. We note that the Tafel parameter $\beta = 0.71$, obtained from a linear fit at the low potentials of Figure 9, takes much larger values in Figure 9 than in Figure 7, mainly due to the effect of the correction of
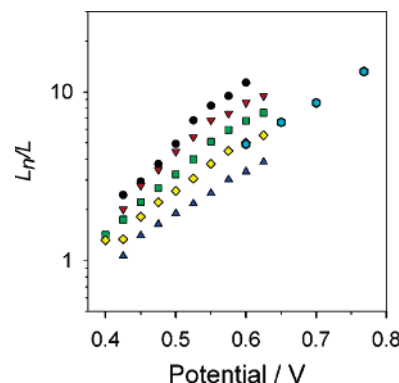
Figure 10. Ratios of the effective diffusion length to the film thickness (L_n/L) of cells A and B at different forward biases and temperatures in the dark.

series resistance in the voltage scale in Figure 9. Excellent agreement is found between the linear approximation of eq 20 and the α-values shown in Table 2.

On another hand, the values obtained from the data fitting for the reorganization energy are in the range of 2 eV, which is much higher than those found in previous works ($\lambda \approx 0.5$ eV), where the direct transfer from the conduction band states was obtained at high voltages.[32,60] However, this is probably an artifact because of the slight curvature obtained at the higher potentials, and the absence of a minimum for R_{ct} yields, as shown in Table 2, a very inaccurate determination of the value of λ. A more systematic investigation of DSC in different conditions of electrolyte and surface treatments is required to clarify the role of the different charge-transfer mechanisms, and this work is in progress.

The competition between the collection and the recombination of electrons can be expressed in terms of the electron diffusion length. The effective diffusion length (L_n) can be expressed as

$$L_n = \sqrt{D_n \tau_n} = L\sqrt{\frac{R_{ct}}{R_t}} = L' \exp\left[\frac{(1-\alpha)e}{2k_B T}V\right] \quad (21)$$

As shown in Figure 10, the obtained L_n increases by about 1 order of magnitude with the bias potential and it becomes larger at lower temperatures, as predicted by eq 21. It is shown that, in the dark and at room temperature, the effective diffusion length of the electrons at 0.65 V is even longer than 100 μm, indicating the excellent transport properties of the mesoscopic TiO$_2$ film. In comparison, cell B has a shorter diffusion length at a similar temperature and bias potential, concordant with the higher position of the conduction band.

It should be noted that the potential dependence of L_n is dramatically different from that obtained under illumination, where the effective diffusion length barely changes with the incident light intensity. The reason lies in the fact that, under illumination, the evolution of R_{ct} is very similar to that of R_t, keeping the validity of eq 8 and, thus, leaving L_n nearly independent of bias light. This behavior is characteristic of DSC as first reported by Peter and co-workers.[21,61−65]

3.3. Correlations between the Impedance Parameters and the Photovoltaic Performance. The following discussions will be focused on the relationship of the impedance parameters to the photovoltaic performance of the cells.[66] The overall conversion efficiency η of the DSC is calculated from the integral photocurrent density (j_{sc}), the open-circuit photovoltage (V_{oc}),

High Efficiency Dye-Sensitized Solar Cells

J. Phys. Chem. B, Vol. 110, No. 50, 2006 **25219**

the fill factor of the cell (ff), and the intensity of the incident light (I_{ph}), namely,

$$\eta = j_{sc}V_{oc}(ff/I_{ph}) \qquad (22)$$

Consequently, the high efficiency of the cell at full sun illumination is given by factors affecting these parameters.

The V_{oc} values of DSC are obtained as the difference between the Fermi level of the electrons in TiO$_2$ in the light and the redox level in the electrolyte, which is almost constant under illumination at open-circuit conditions. Consequently, the establishment of a high Fermi level from the balance between the charge injection in TiO$_2$ and the recombination to I$_3^-$ in the electrolyte is the central factor for a high photovoltage. In this sense, the relatively high values of R_{ct} and C_μ that yield the excellent value of lifetime τ_n (>100 ms at high bias potential) contribute to keeping V_{oc} at a high level by avoiding electron loss in the semiconductor. Furthermore, the high recombination resistance, even at the highest potentials studied, is reduced only moderately under illumination. For example, the R_{ct} of cell B is reduced by only 25% under 0.1 sun illumination (0.768 V) and this decrease in R_{ct} also seems to occur at 1 sun illumination, by ~45%.

An additional contribution to the high V_{oc} of cell B is given by the higher position of the TiO$_2$ conduction band that, at the same time, maintains excellent electron injection from the excited dye molecules. This is a key reason for these highly efficient DSC. It is generally accepted that the potential-determining ions in the electrolyte have a major impact on the conduction band position of TiO$_2$.[15,23,67−70] Here, the presence of guanidinium cation in the electrolyte and its interaction with TiO$_2$ or other potential-determining ions are believed to be responsible for this. However, the detailed mechanism needs further study.

The short-circuit photocurrent is another parameter that is fundamental to the efficiency of DSC. First of all, a good charge-injection efficiency from the excited dye to TiO$_2$ is basic for this. For the Ru-complex used here, it has been proved in many papers[71−78] that the injection from the excited molecule to the conduction band of the semiconductor is fast enough to compete with other processes (almost unity IPCE). So, the charge collection/extraction efficiency of the injected electron is critical to the photocurrent of the cell. The effective diffusion length of the charge in a TiO$_2$ film is widely accepted to be a good indicator for charge extraction. As shown in Figure 10, L_n is much longer than the film thickness, especially at a high bias potential. The excellent charge-transport property and the large recombination resistance, in conjunction with the large rate of injection from the dye, provide the good photocurrents of these cells even though the conduction band on TiO$_2$ (and thus the photovoltage) is rather high. The difference between the positions of the conduction band is believed to be the main reason to explain the difference between the j_{sc} values of cells A and B.[15,23,68−70]

In addition, the good fill factor is an important reason for the high efficiency. A low total series resistance of these cells contributes to the good ff value. The series resistance can be expressed as a sum of the different contributions:

$$R_{Stot} = R_S + R_{Pt} + R_{CO} + \frac{1}{3}R_t + R_D \qquad (23)$$

It was found that these cells presented smaller R_{Stot} values than other small-size solar cells with lower efficiencies and that cell B had half of the R_{Stot} of cell A. This fact explains the better ff
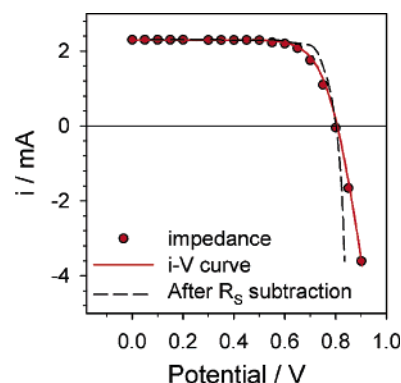
Figure 11. Photocurrent−voltage curve of cell A obtained at AM 1.5 solar radiation. The dots show the calculated values based on the impedance measurements carried out at different voltage biases of the cell with the same illumination. The dashed line represents the simulated curve after subtraction of the series resistance. A 10% increase in the fill factor is obtained.

value found for the first one.[79] Moreover, the fill factor is also limited by the transfer coefficient β of electron transfer from TiO$_2$ to the electrolyte. It has been shown in another work that, at a given V_{oc}, the larger the β value, the better the fill factor.[79] According to the model outlined above, in eq 20, the larger β value is associated with a smaller T_0 value, which means a shallower distribution of the surface states. Thus, the higher fill factor of cell B in comparison with cell A is partly due to the relatively higher transfer coefficient. The influence of the transfer coefficient on the fill factor implies that the preparation of a TiO$_2$ film with an optimum surface state distribution is critical for obtaining high-performance DSC.

Finally, the $i-V$ curve of the cell can be reproduced with the parameters obtained by impedance measurements under illumination. Taking into account that the total resistance is the sum of all the contributions,

$$R_{tot} = R_{Stot} + R_{ct} \qquad (24)$$

we can obtain the current flowing through the cell at a certain potential V by using the short circuit photocurrent I_{sc} through[79]

$$i = I_{sc} - \int_0^V \frac{dV}{R_{tot}} \qquad (25)$$

By taking the I_{SC} of cell A under 1 sun illumination, Figure 11 reveals the $i-V$ data of the cell deduced from the impedance measurements and the comparison with the curve obtained from the voltammetric measurements. It shows that the impedance data fit very well to the voltammetric curve, suggesting, on the other hand, the validity and reliability of the impedance measurements.

A major contribution to series resistance is given by the sheet resistance of TCO, and it could be diminished with a better design of the sample. Also, R_{Pt} may be lowered by increasing the porosity of the deposit at the counter electrode and R_D may be lowered by increasing the conductivity of the electrolyte and moving the counter electrode closer to the TiO$_2$ film. The potential effect of such improvements is shown by the dashed line in Figure 11 that simulates the $i-V$ curve after complete subtraction if $R_{Stot}:ff$ increases by 10%.

4. Conclusions

Impedance spectroscopy has been demonstrated to be a very helpful technique to investigate the electron transport and recombination mechanisms of DSC in this study. The measure-

25220 *J. Phys. Chem. B, Vol. 110, No. 50, 2006*

Wang et al.

ments have also allowed an insight into the origins of the high efficiency of the cells.

The analysis of the impedance parameters at different bias potentials, that is, at different electron Fermi levels, shows that the exponential distribution of the localized states in the band gap of the TiO_2 nanoparticles plays a dominant role in charge accumulation, transport, and recombination. All of the associated parameters, that is, the chemical capacitance, the steady-state transport resistance, the transient diffusion coefficient, and the charge-transfer (recombination) resistance, have been interpreted in a unified and consistent framework. By changing the temperature and bias potential of the cell, the diffusion coefficient has been shown to exhibit the behavior expected in the multiple trapping model of electron transport within mesoscopic TiO_2 films. Electrons in the localized states within the band gap of TiO_2 transport through trapping and detrapping processes between the trap states and the conduction band, and only free electrons in the conduction band edge contribute to the steady-state diffusion process. With respect to the interfacial charge recombination process, the behavior of recombination resistance versus bias potential suggest a surface state-mediated charge-transfer mechanism within the studied potential range. However, the charge-transfer mechanism remains the most complex aspect of the DSC and requires further investigation. In addition, the transport mechanism at the transport level has not been separately observed.

It can be concluded from the impedance measurements that the high efficiency of the cells in this study is ascribed to the excellent transport and low recombination rate of electrons in TiO_2. It was shown that a high conduction band position that also maintains excellent electron injection from the excited dye molecules is the key reason for these highly efficient DSC. The high quality of the mesoscopic TiO_2 film and the optimized TiO_2–electrolyte interface are believed to be responsible for this. In addition, the low series resistance and an optimum distribution of the surface states in TiO_2 result in an excellent fill factor.

Supporting Information Available: Arrhenius plots of electron transport resistance R_t and recombination resistance R_{ct} of cell **A** at various bias potentials. This material is available free of charge via the Internet at http://pubs.acs.org.

References and Notes

(1) O'Regan, B.; Grätzel, M. *Nature* **1991**, *353*, 737.

(2) Nazeeruddin, M. K.; Kay, A.; Rodicio, I.; Humphry-Baker, R.; Müller, E.; Liska, P.; Vlachopoulas, N.; Grätzel, M. *J. Am. Chem. Soc.* **1993**, *115*, 6382.

(3) Nazeeruddin, M. K.; Pechy, P.; Renouard, T.; Zakeeruddin, S. M.; Humphry-Baker, R.; Comte, P.; Liska, P.; Cevey, L.; Costa, E.; Shklover, V.; Spiccia, L.; Deacon, G. B.; Bignozzi, C. A.; Grätzel, M. *J. Am. Ceram. Soc.* **2001**, *123*, 1613.

(4) Wang, P.; Zakeeruddin, S. M.; Moser, J. E.; Nazeeruddin, M. K.; Sekiguchi, T.; Grätzel, M. *Nat. Mater.* **2003**, *2*, 402.

(5) Bisquert, J.; Cahen, D.; Rühle, S.; Hodes, G.; Zaban, A. *J. Phys. Chem. B* **2004**, *108*, 8106.

(6) Grätzel, M. *Inorg. Chem.* **2005**, *44*, 6841.

(7) Nazeeruddin, M. K.; De Angelis, F.; Fantacci, S.; Selloni, A.; Viscardi, G.; Liska, P.; Ito, S.; Takeru, B.; Grätzel, M. *J. Am. Chem. Soc.* **2005**, *127*, 16835.

(8) Nazeeruddin, M. K.; Grätzel, M. *J. Photochem. Photobiol., A* **2001**, *145*, 79.

(9) Hauch, A.; Georg, A. *Electrochim. Acta* **2001**, *46*, 3457.

(10) Bisquert, J. *J. Phys. Chem. B* **2002**, *106*, 325.

(11) Kern, R.; Sastrawan, R.; Ferber, J.; Stangl, R.; Luther, J. *Electrochim. Acta* **2002**, *47*, 4213.

(12) Fabregat-Santiago, F.; Garcia-Belmonte, G.; Bisquert, J.; Zaban, A.; Salvador, P. *J. Phys. Chem. B* **2002**, *106*, 334.

(13) Bisquert, J.; Vikhrenko, V. S. *J. Phys. Chem. B* **2004**, *108*, 2313.

(14) Bisquert, J. *Phys. Chem. Chem. Phys.* **2003**, *5*, 5360.

(15) Fabregat-Santiago, F.; Bisquert, J.; Garcia-Belmonte, G.; Boschloo, G.; Hagfeldt, A. *Sol. Energy Mater. Sol. Cells* **2005**, *87*, 117.

(16) Wang, Q.; Moser, J. E.; Grätzel, M. *J. Phys. Chem. B* **2005**, *109*, 14945.

(17) Hoshikawa, T.; Kikuchi, R.; Eguchi, K. *J. Electroanal. Chem.* **2006**, *588*, 59.

(18) Adachi, M.; Sakamoto, M.; Jiu, J.; Ogata, Y.; Isoda, S. *J. Phys. Chem. B* **2006**, *110*, 13872.

(19) van de Lagemaat, J.; Frank, A. J. *J. Phys. Chem. B* **2001**, *105*, 11194.

(20) van de Lagemaat, J.; Kopidakis, N.; Neale, N. R.; Frank, A. J. *Phys. Rev. B* **2005**, *71*, 035304.

(21) Fisher, A. C.; Peter, L. M.; Ponomarev, E. A.; Walker, A. B.; Wijayantha, K. G. U. *J. Phys. Chem. B* **2000**, *104*, 949.

(22) Hara, K.; Miyamoto, K.; Abe, Y.; Yanagida, M. *J. Phys. Chem. B* **2005**, *109*, 23776.

(23) Schlichthröl, G.; Huang, S. Y.; Sprague, J.; Frank, A. J. *J. Phys. Chem. B* **1997**, *101*, 8141.

(24) Nazeeruddin, M. K.; Zakeeruddin, S. M.; Humphry-Baker, R.; Jirousek, M.; Liska, P.; Vlachopoulos, N.; Shklover, V.; Fischer, C. H.; Grätzel, M. *Inorg. Chem.* **1999**, *38*, 6298.

(25) Bonhôte, P.; Dias, A.-P.; Papageorgious, N.; Kalyanasundaraman, K.; Grätzel, M. *Inorg. Chem.* **1996**, *35*, 1168.

(26) Wang, P.; Zakeeruddin, S. M.; Comte, P.; Charvet, R.; Humphry-Baker, R.; Grätzel, M. *J. Phys. Chem. B* **2003**, *107*, 14336.

(27) Ito, S.; Matsui, H.; Okada, K.; Kusano, S.; Kitamura, T.; Wada, Y.; Yanagida, S. *Sol. Energy Mater. Sol. Cells* **2004**, *82*, 421−429.

(28) Koide, N.; Han, L. Y. *Rev. Sci. Instrum.* **2004**, *75*, 2828.

(29) Chiba, Y.; Islam, A.; Watanabe, Y.; Komiya, R.; Koide, N.; Han, L. *Jpn. J. Appl. Phys., Part 2* **2006**, *45*, 24−28.

(30) Wei, M.; Konishi, Y.; Zhou, H.; Yanagida, M.; Sugihara, H.; Arakawa, H. *J. Mater. Chem.* **2006**, *16*, 1287.

(31) Bisquert, J. *Phys. Chem. Chem. Phys.* **2003**, *5*, 5360.

(32) Bisquert, J.; Zaban, A.; Greenshtein, M.; Mora-Seró, I. *J. Am. Chem. Soc.* **2004**, *126*, 13550.

(33) Fabregat-Santiago, F.; Mora-Seró, I.; Garcia-Belmonte, G.; Bisquert, J. *J. Phys. Chem. B* **2003**, *107*, 758.

(34) Peter, L. M.; Duffy, N. W.; Wang, R. L.; Wijayantha, K. G. U. *J. Electroanal. Chem.* **2002**, *524−525*, 127.

(35) Howe, R.; Grätzel, M. *J. Phys. Chem.* **1985**, *89*, 4495.

(36) Fabregat-Santiago, F.; Mora-Seró, I.; Garcia-Belmonte, G.; Bisquert, J. *J. Phys. Chem. B* **2003**, *107*, 758.

(37) Zhang, Z.; Zakeeruddin, S. M.; O'Regan, B. C.; Humphry-Baker, R.; Grätzel, M. *J. Phys. Chem. B* **2005**, *109*, 21818.

(38) Niinobe, D.; Makari, Y.; Kitamura, T.; Wada, Y.; Yanagida, S. *J. Phys. Chem. B* **2005**, *109*, 17892.

(39) Movilla, J. L.; Garcia-Belmonte, G.; Bisquert, J.; Planelles, J. *Phys. Rev. B* **2005**, *72*, 153313.

(40) Abayev, I.; Zaban, A.; Kytin, V. G.; Danilin, A. A.; Garcia-Belmonte, G.; Bisquert, J. *J. Solid State Electrochem.*, in press.

(41) Kopidakis, N.; Neale, N. R.; Zhu, K.; van de Lagemaat, J.; Frank, A. J. *Appl. Phys. Lett.* **2005**, *87*, 202106.

(42) Olson, C. L.; Nelson, J.; Islam, M. S. *J. Phys. Chem. B* **2006**, *110*, 9995.

(43) Mora-Seró, I.; Bisquert, J.; Fabregat-Santiago, F.; Garcia-Belmonte, G.; Zoppi, G.; Durose, K.; Proskuryakov, Y.; Oja, I.; Belaidi, A.; Dittrich, T.; Tena-Zaera, R.; Katty, A.; Levy-Clement, C.; Barrioz, V.; Irvine, S. J. C. *Nano Lett.* **2006**, *6*, 640.

(44) Tiedje, T.; Rose, A. *Solid State Commun.* **1981**, *37*, 49.

(45) Bisquert, J. *J. Phys. Chem. B* **2004**, *108*, 2323.

(46) Nakade, S.; Saito, Y.; Kubo, W.; Kitamura, T.; Wada, Y.; Yanagida, S. *J. Phys. Chem. B* **2003**, *107*, 8607.

(47) Fabregat-Santiago, F.; García-Cañadas, J.; Palomares, E.; Clifford, J. N.; Haque, S. A.; Durrant, J. R.; Garcia-Belmonte, G.; Bisquert, J. *J. Appl. Phys.* **2004**, *96*, 6903.

(48) Kopidakis, N.; Neale, N. R.; Zhu, K.; van de Lagemaat, J.; Frank, A. J. *Appl. Phys. Lett.* **2005**, *87*, 202106.

(49) Kopidakis, N.; Benkstein, K. D.; van de Lagemaat, J.; Frank, A. J.; Yuan, Q.; Schiff, E. A. *Phys. Rev. B* **2006**, *73*, 045326.

(50) Orenstein, J.; Kastner, M. *Phys. Rev. Lett.* **1981**, *46*, 1421.

(51) Schlichthörl, G.; Huang, S. Y.; Sprague, J.; Frank, A. J. *J. Phys. Chem. B* **1997**, *101*, 8141.

(52) Abayev, I.; Zaban, A.; Fabregat-Santiago, F.; Bisquert, J. *Phys. Status Solidi A* **2003**, *196*, R4.

(53) Forro, L.; Chauvet, O.; Emin, D.; Zuppiroli, L.; Nerger, H.; Lévy, F. *J. Appl. Phys.* **1994**, *75*, 633.

(54) Tang, H.; Prasad, K.; Sanjinès, R.; Schmid, P. E.; Lévy, F. *J. Appl. Phys.* **1994**, *75*, 2042.

(55) Turner, G. M.; Beard, M. C.; Schmuttenmaer, C. A. *J. Phys. Chem. B* **2002**, *106*, 11716.

(56) Hendry, E.; Koeberg, M.; O'Regan, B.; Bonn, M. *Nano Lett.* **2006**, *6*, 755.

(57) Kroeze, J. E.; Savenije, T. J.; Warman, J. M. *J. Am. Chem. Soc.* **2004**, *126*, 7608.

(58) Kroeze, J. E.; Savenije, T. J.; Warman, J. M.; Vermeulen, M. J. W. *J. Phys. Chem. B* **2003**, *107*, 7696.

(59) Bisquert, J.; Zaban, A.; Salvador, P. *J. Phys. Chem. B* **2002**, *106*, 8774.

(60) Salvador, P.; González-Hidalgo, M.; Zaban, A.; Bisquert, J. *J. Phys. Chem. B* **2005**, *109*, 15915.

(61) Krüger, J.; Plass, R.; Grätzel, M.; Cameron, P. J.; Peter, L. M. *J. Phys. Chem. B* **2003**, *107*, 7536.

(62) Peter, L. M.; Wijayantha, K. G. U. *Electrochim. Acta* **2000**, *45*, 4543.

(63) Schlichthörl, G.; Park, N. G.; Frank, A. J. *J. Phys. Chem. B* **1999**, *103*, 782.

(64) Peter, L. M.; Ponomarev, E. A.; Walker, A. B.; Wijayantha, K. G. U. *Electrochem. Commun.* **1999**, *1*, 576.

(65) Frank, A. J.; Kopidakis, N.; van de Lagemaat, J. *Coord. Chem. Rev.* **2004**, *248*, 1165.

(66) Mora-Seró, I.; Bisquert, J.; Fabregat-Santiago, F.; Garcia-Belmonte, G.; Zoppi, G.; Durose, K.; Proskuryakov, Y.; Oja, I.; Belaidi, A.; Dittrich, T.; Tena-Zaera, R.; Katty, A.; Lévy-Clement, C.; Barrioz, V.; Irvine, S. J. C. *Nano Lett.*, in press.

(67) Kopidakis, N.; Benkstein, K. D.; van de Lagemaat, J.; Frank, A. J. *J. Phys. Chem. B* **2003**, *107*, 11307.

(68) Huang, S. Y.; Schilchthörl, G.; Nozik, A. J.; Grätzel, M.; Frank, A. J. *J. Phys. Chem. B* **1997**, *101*, 2576.

(69) Hara, K.; Dan-Oh, Y.; Kasada, C.; Ohga, Y.; Shinpo, A.; Suga, S.; Sayama, K.; Arakawa, H. *Langmuir* **2004**, *20*, 4205.

(70) Liu, Y.; Hagfeldt, A.; Xiao, X.-R.; Lindquist, S.-E. *Sol. Energy Mater. Sol. Cells* **1998**, *55*, 267.

(71) Tachibana, Y.; Moser, J. E.; Grätzel, M.; Klug, D. R.; Durrant, J. R. *J. Phys. Chem.* **1996**, *100*, 200556.

(72) Asbury, J. B.; Hao, E.; Wang, Y.; Ghosh, H. N.; Lian, T. *J. Phys. Chem. B* **2001**, *105*, 4545.

(73) Tachibana, Y.; Haque, S. A.; Mercer, I. P.; Moser, J. E.; Klug, D. R.; Durrant, J. R. *J. Phys. Chem. B* **2001**, *105*, 7424.

(74) Huber, R.; Sporlein, S.; Moser, J. E.; Grätzel, M.; Wachtveitl, J. *J. Phys. Chem. B* **2000**, *104*, 8995.

(75) Kallioinen, J.; Benko, G.; Sundstrom, V.; Korppi-Tommola, J. E. I.; Yartsev, A. P. *J. Phys. Chem. B* **2002**, *106*, 4396.

(76) Asbury, J. B.; Anderson, N. A.; Hao, E. C.; Ai, X.; Lian, T. Q. *J. Phys. Chem. B* **2003**, *107*, 7376.

(77) Persson, P.; Lundqvist, M. J. *J. Phys. Chem. B* **2005**, *109*, 11918.

(78) Wenger, B.; Grätzel, M.; Moser, J. E. *Chimia* **2005**, *59*, 123.

(79) Fabregat-Santiago, F.; Bisquert, J.; Palomares, E.; Zakeeruddin, M.; Grätzel, M. In preparation.